ORIGINAL PAPER

Simulation of axis-symmetric seismic waves in fluid-filled boreholes in the presence of a drill string

Simulation of axis-symmetric seismic waves

José M. Carcione · Flavio Poletto · Biancamaria Farina

Abstract A numerical algorithm for simulation of *2-D (axis-symmetric)* wave propagation using a multidomain approach is proposed. The method uses a cylindrical coordinate system, Chebyshev and Fourier differential operators to calculate the spatial derivatives along the radial and vertical direction, respectively, and a Runge–Kutta time-integration scheme. The numerical technique is based on the solution of the equations of momentum conservation combined with the stress–strain relations of the fluid (drilling mud) and isotropic elastic media (drill string and formation). Wave modes and radiated waves are simulated in the borehole-formation system. The algorithm satisfies the reciprocity condition and the results agree with an analytical solution and low-frequency simulation of wave-propagation modes reported in the literature. Examples illustrating the propagation of waves are presented for hard and soft formations. Moreover, the presence of casing, cement, and formation heterogeneity have been considered. Since the algorithm is based on a direct (grid) method, the geometry and the properties defining the media at each grid point, can be general, i.e., there are no limitations such as planar interfaces or uniform (homogeneous) properties for each medium.

J. M. Carcione (✉) · F. Poletto · B. Farina
Istituto Nazionale di Oceanografia e di Geofisica
Sperimentale (OGS), Borgo Grotta Gigante 42c,
34010 Sgonico, Trieste, Italy
e-mail: jcarcione@inogs.it

1 Introduction

The extraction of hydrocarbons and geothermal resources from the Earth's crust requires the drilling of deep wells. Seismic while drilling is a recent technology that uses the extensional wave generated at the drill bit and detected at the rig to obtain reverse vertical-seismic-profile (VSP) seismograms [18]. This pilot signal is used to process the data acquired at the surface by a seismic survey. Moreover, drill-string guided waves contain information about the drilling conditions and can be used to transmit data from downhole to the surface. Other borehole signals that can be used to transmit information to the surface are the low-frequency Stoneley wave traveling between the mud and the formation (the so-called tube waves), and the wave traveling inside the drill pipes, filled with drilling mud. The velocity of these guided waves depends on the drilling-mud properties, the elastic properties of the surrounding formation, the borehole lateral dimensions, and the drill-string properties and geometry. Hence, understanding wave propagation in boreholes with a drill-pipe is important for a correct data processing and for designing optimal acquisition parameters.

Lee [13] and Lea and Killingstad [12] consider the drill-string/borehole system with the inner and outer drilling mud. They compute the velocities of the different wave modes by using a low-frequency

approximation and conclude that wave coupling is important, mainly between the fluid modes (inner and annular pressure waves). Rama Rao and Vandiver [19] analyze the acoustic properties of a water-filled borehole with pipes, calculating the axis-symmetric propagation of the different modes for frequencies less than 1 kHz, and considering soft and hard formations.

A relatively simple 1-D modeling algorithm has been proposed by Carcione and Poletto [8], who have solved the differential equations describing wave propagation through the drill string. They compute waveforms of the extensional, torsional, and flexural waves by modeling the geometrical features of the coupling joints, including piezoelectric sources and sensors.

The approach proposed here generalizes the method of Lee [13] and Lea and Kyllingstad [12] in that (1) it is not restricted to the low-frequency approximation; (2) it gives the heterogeneous differential equations of motion, i.e., the equations are not restricted to a uniform drill string; (3) the algorithm gives the full-wave solution, without approximations, such as neglecting the shear stress σ_{rz}; and (4) it considers the formation and other layers such as the borehole casing and cement. Our algorithm simulates 3-D axis-symmetric waves in a 2-D multidomain and it is based on a pseudospectral expansion of the solution in the spatial coordinates and a *Taylor* method time-integration scheme. The radial spatial derivatives are computed with the Chebyshev method, the vertical spatial derivatives are computed with the Fourier method, and the integration in time is carried out using the fourth-order Runge–Kutta algorithm (e.g., [2, 6]). The algorithm uses four meshes, corresponding, in principle, to the inner mud, drill string, outer mud, and casing/formation media (Fig. 1 shows a vertical section of the borehole). Vertical variations of the drill string section, such as those due to the presence of coupling joints, are modeled by setting the properties of the drilling mud to the relevant grid points associated with the drill string. Variations of the hole diameter are treated in a similar way. Two adjacent meshes are combined by decomposing the wave fields into incoming and outgoing wave modes at the interface between the media and modifying these modes on the basis of the fluid/solid boundary conditions [3].

This method can also be used to simulate synthetic logs at the sonic frequency range [20], and reverse vertical-seismic profiles. The problem of obtaining a realistic VSP survey by using pseudospectral differential operators was considered by Kessler and Kosloff in two papers [14, 15]. They solve for 2-D acoustic and elastic wave propagation in a (horizontal) plane *perpendicular to the axis of symmetry of the hole* by using Chebychev and Fourier differential operators in the radial and
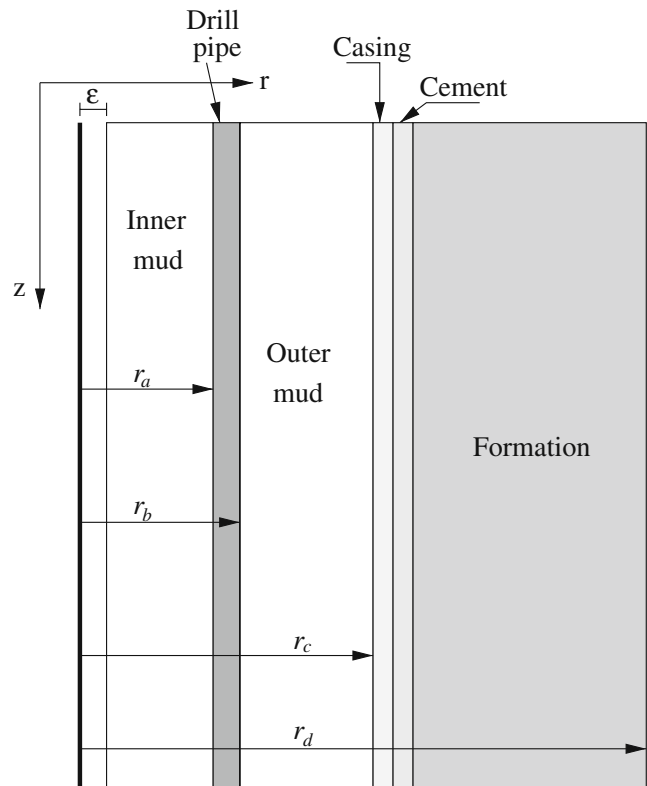
Fig. 1 Diagram showing a section of the borehole–drill-string–formation system used in the simulation of propagation modes. The ranges of the four meshes are $r_a - \epsilon$ for the inner mud (ϵ is the minimum radius of the inner mesh), $r_b - r_a$ for the drill-string, $r_c - r_b$ for the outer mud, and $r_d - r_c$ for the casing–cement–formation system

angular directions, respectively. We are considering the simulation in a vertical plane. Therefore, the present work is a first step to achieve a complete 3-D simulation.

2 Equations of momentum conservation

We consider the constitutive equations for solid and fluid layers. The axis-symmetric 3-D equations of momentum conservation in cylindrical coordinates for the solid (i.e., pipe, casing, and formation) can be expressed as [10]

$$\rho \dot{v}_r = \frac{1}{r} \frac{\partial}{\partial r} (r \sigma_{rr}) + \frac{\partial \sigma_{rz}}{\partial z} - \frac{\sigma_{\theta\theta}}{r} + f_r, \qquad (1)$$

$$\rho \dot{v}_z = \frac{1}{r} \frac{\partial}{\partial r} (r \sigma_{rz}) + \frac{\partial \sigma_{zz}}{\partial z} + f_z, \qquad (2)$$

where r, θ, and z are the spatial variables, ρ is the density, the σ values are stress components, the v values are particle velocities, and the f values are body forces

per unit volume. A dot above a variable denotes time differentiation.

The corresponding equations for the fluid (drilling mud) are

$$\rho \dot{v}_r = \frac{\partial \sigma_{\text{rr}}}{\partial r}, \tag{3}$$

$$\rho \dot{v}_z = \frac{\partial \sigma_{\text{rr}}}{\partial z}, \tag{4}$$

where $-\sigma_{\text{rr}}$ is the fluid pressure and the external dilatational source is incorporated in the constitutive relation (see Eq. 9).

3 Stress–strain relations

The 3-D stress–strain relations for the solid are given by

$$\dot{\sigma}_{\text{rr}} = (\lambda + 2\mu)\frac{\partial v_r}{\partial r} + \lambda \left(\frac{\partial v_z}{\partial z} + \frac{v_r}{r} \right), \tag{5}$$

$$\dot{\sigma}_{\theta\theta} = \lambda \left(\frac{\partial v_r}{\partial r} + \frac{\partial v_z}{\partial z} \right) + (\lambda + 2\mu)\frac{v_r}{r}, \tag{6}$$

$$\dot{\sigma}_{zz} = (\lambda + 2\mu)\frac{\partial v_z}{\partial z} + \lambda \left(\frac{\partial v_r}{\partial r} + \frac{v_r}{r} \right), \tag{7}$$

$$\dot{\sigma}_{rz} = \mu \left(\frac{\partial v_r}{\partial z} + \frac{\partial v_z}{\partial r} \right), \tag{8}$$

where λ and μ are the Lamé constants. These constants are related to the P-wave and S-wave velocities (v_P and v_S) by $\lambda = \rho(v_P^2 - 2v_S^2)$ and $\mu = \rho v_S^2$.

The corresponding constitutive equation for the fluid is

$$\dot{\sigma}_{\text{rr}} = \lambda \left(\frac{\partial v_r}{\partial r} + \frac{\partial v_z}{\partial z} + \frac{v_r}{r} \right) + \dot{f}_{\text{rr}}, \tag{9}$$

where f_{rr} is a dilatational source.

4 Domain decomposition and boundary conditions

The solution on each grid is obtained by using a *fourth-order* Runge–Kutta method as time stepping algorithm, the Chebyshev differential operator [4, 6] to compute the spatial derivatives along the radial direction and the Fourier differential operator [6] along the vertical direction. The Fourier and Chebyshev operators have spectral accuracy and, therefore, avoid numerical dispersion, which is a characteristic feature of low-order

schemes. In fact, the existing modeling schemes have finite accuracy due to the low-order approximations of the time and space derivatives since they are mostly based on finite-difference and finite-element methods. The pseudospectral operators are infinitely accurate for band-limited periodic functions with cutoff spatial wavenumbers smaller than the cutoff wavenumbers of the mesh [6, 9]. Moreover, they use two points per minimum wavelength, allowing minimum computer storage requirements, mainly in 3-D space. Another advantage is the accurate modeling of surface and interface waves [7], since the Chebyshev collocation points are denser at the edges of the mesh. The use of characteristics allows us to simulate Dirichlet, Neumann, and nonreflecting boundary conditions [4]. This versatility makes the Chebyshev differentiation very accurate for domain decomposition problems, such as the case of fluid–solid interfaces [7]. To our knowledge, finite difference methods have not been used to describe such interfaces with domain decomposition. Both spatial derivatives are computed using the fast Fourier transform, which can be vectorized and can run efficiently in parallel computers.

The Gauss–Lobatto collocation points *corresponding to the Chebyshev operator* are defined as $r_i = -\cos[\pi(i-1)/(n_r - 1)]$, $i = 1, \ldots, n_r$, where n_r is the number of radial grid points. Two adjacent meshes are combined by decomposing the wave field into incoming and outgoing wave modes at the interface between the media and modifying these modes on the basis of the fluid/solid boundary conditions [6]. The inward propagating waves depend on the solution exterior to the subdomains and, therefore, are computed from the boundary conditions (continuity of stress and particle-velocity components), while the behavior of the outward propagating waves is determined by the solution inside the subdomain [3, 5, 15]. The approach involves the following equations for updating the field variables at the grid points defining the interface between the fluid and the solid, such that *the upper sign corresponds to fluid* (1) */solid* (2) *and the lower sign to solid* (1)/ *fluid* (2):

$$\begin{aligned} v_r^{(\text{new})}(1, 2) = {} & \frac{1}{Z_P(1) + Z_P(2)} \\ & \times \left[Z_P(1)v_r^{(\text{old})}(1) + Z_P(2)v_r^{(\text{old})}(2) \right. \\ & \left. \pm \sigma_{\text{rr}}^{(\text{old})}(1) \mp \sigma_{\text{rr}}^{(\text{old})}(2) \right], \end{aligned} \tag{10}$$

$$v_z^{(\text{new})} = v_z^{(\text{old})} \mp \frac{1}{Z_S}\sigma_{rz}^{(\text{old})} \text{ (solid)}, \quad v_z^{(\text{new})} = v_z^{(\text{old})} \text{ (fluid)}, \tag{11}$$

$$\sigma_{\mathrm{rr}}^{(\mathrm{new})}(1,2) = \frac{Z_P(1)Z_P(2)}{Z_P(1)+Z_P(2)}$$
$$\times \left[\pm v_r^{(\mathrm{old})}(1) \mp v_r^{(\mathrm{old})}(2) + \frac{1}{Z_P(1)}\sigma_{\mathrm{rr}}^{(\mathrm{old})}(1) \right.$$
$$\left. + \frac{1}{Z_P(2)}\sigma_{\mathrm{rr}}^{(\mathrm{old})}(2) \right], \tag{12}$$

$$\sigma_{\theta\theta}^{(\mathrm{new})} = \sigma_{\theta\theta}^{(\mathrm{old})} + \frac{\lambda}{(\lambda+2\mu)}\left[\sigma_{\mathrm{rr}}^{(\mathrm{new})} - \sigma_{\mathrm{rr}}^{(\mathrm{old})}\right], \tag{13}$$

$$\sigma_{zz}^{(\mathrm{new})} = \sigma_{zz}^{(\mathrm{old})} + \frac{\lambda}{(\lambda+2\mu)}\left[\sigma_{\mathrm{rr}}^{(\mathrm{new})} - \sigma_{\mathrm{rr}}^{(\mathrm{old})}\right], \tag{14}$$

$$\sigma_{rz}^{(\mathrm{new})} = 0, \tag{15}$$

where $Z_P = \rho v_P$ and $Z_S = \rho v_S$. The upper signs correspond to the inner mud (1)/string (2) and outer mud (1)/casing (2) interfaces, and the lower signs correspond to the string (1)/outer mud (2) interface.

Because of the singularity at the hole axes ($r = 0$), we choose the inner radius, ϵ, of the inner mesh (inner mud) different from zero and small with respect to the wavelength. This boundary satisfies the following free-surface boundary conditions:

$$v_r^{(\mathrm{new})} = v_r^{(\mathrm{old})} - \sigma_{\mathrm{rr}}^{(\mathrm{old})}/Z_P, \tag{16}$$

$$v_z^{(\mathrm{new})} = v_z^{(\mathrm{old})}, \tag{17}$$

$$\sigma_{\mathrm{rr}}^{(\mathrm{new})} = 0. \tag{18}$$

The outer boundary of the outer grid (formation) satisfies the following nonreflecting boundary conditions:

$$v_r^{(\mathrm{new})} = 0.5\left(v_r^{(\mathrm{old})} + \sigma_{\mathrm{rr}}^{(\mathrm{old})}/Z_P\right), \tag{19}$$

$$v_z^{(\mathrm{new})} = 0.5\left(v_z^{(\mathrm{old})} + \sigma_{rz}^{(\mathrm{old})}/Z_S\right), \tag{20}$$

$$\sigma_{\mathrm{rr}}^{(\mathrm{new})} = 0.5\left(\sigma_{\mathrm{rr}}^{(\mathrm{old})} + Z_P v_r^{(\mathrm{old})}\right), \tag{21}$$

$$\sigma_{rz}^{(\mathrm{new})} = 0.5\left(\sigma_{rz}^{(\mathrm{old})} + Z_S v_z^{(\mathrm{old})}\right), \tag{22}$$

$$\sigma_{\theta\theta}^{(\mathrm{new})} = \sigma_{\theta\theta}^{(\mathrm{old})} + \frac{\lambda}{E}\left(\sigma_{\mathrm{rr}}^{(\mathrm{new})} - \sigma_{\mathrm{rr}}^{(\mathrm{old})}\right), \tag{23}$$

$$\sigma_{zz}^{(\mathrm{new})} = \sigma_{zz}^{(\mathrm{old})} + \frac{\lambda}{E}\left(\sigma_{\mathrm{rr}}^{(\mathrm{new})} - \sigma_{\mathrm{rr}}^{(\mathrm{old})}\right), \tag{24}$$

Absorbing strips are added to attenuate further the wave field at the outer boundary and also at the top and the bottom of all meshes [4].

5 Simulations

An example of multimesh is shown in Fig. 2, where the location of the grid points in the radial direction can be seen. The thicker lines correspond to the interfaces between the media. The shown multimeshes model uses $n_r = 11$, 11, 11, and 76 grid points in the radial direction for the inner mud, drill string, outer mud, and formation, respectively.

5.1 Comparison between numerical and analytical solution

To test the algorithm and, particularly, the effectiveness of the boundary condition at the origin ($r = \epsilon$), we compare the numerical and analytical solutions for acoustic axis-symmetric propagation in a homogeneous fluid (mud) with compressional velocity $v_P = 1{,}558$ m/s and density $\rho = 1$ g/cm^3. The models corresponding
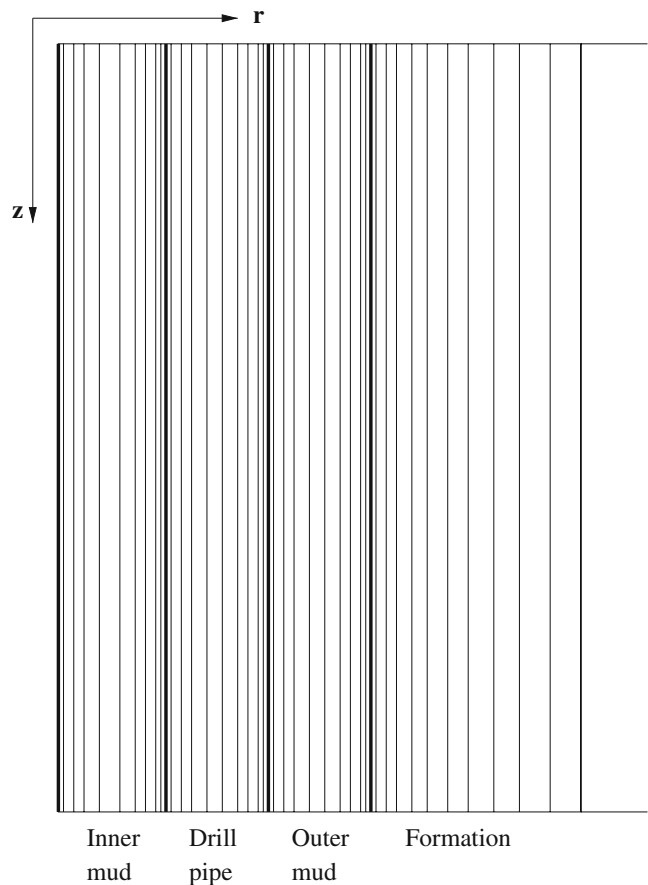
Fig. 2 Example of multimesh showing the location of the grid points in the radial direction. The *thicker lines* correspond to the interfaces between the media. Some points corresponding to the formation are shown
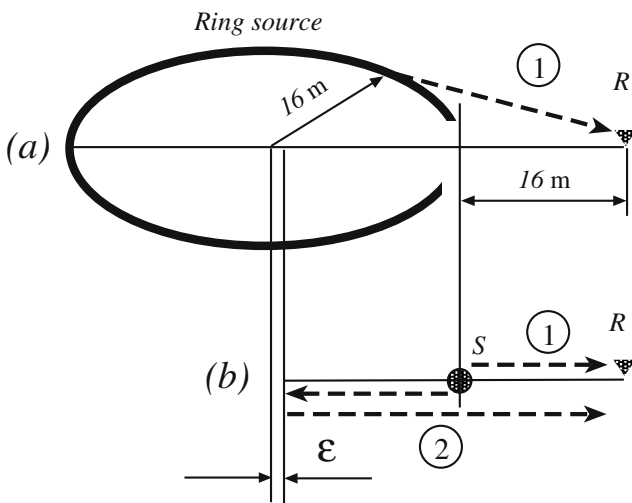
Fig. 3 Models corresponding to the analytical (*a*) and numerical (*b*) solutions. The *dashed lines* represent the paths of the signals from the source *S* to the receiver *R*. *1* is the direct arrival and *2* is the signal reflected at the inner boundary ($r = \epsilon$). In *a*, there is no reflection from the origin

to the analytical and numerical solutions are shown in Fig. 3.

To calculate the analytical solution, we consider a ring source composed of *N* point sources. The radius of the ring is $r_0 = 16$ m. The analytical signal at the receiver, located at 32 m from the ring center, is the linear superposition of *Green's functions* of all the point sources.

Each Green's function only depends on the distance *r* from the singular point source to the receiver and is obtained by combining Newton's Eq. 3 and 4 and Hooke's law (Eq. 9), where $f_{rr}(t, r) = g(t)\delta(r)$ with δ *Dirac's function*. We obtain

$$\left(\Delta - \frac{1}{c^2}\partial_{tt}\right)\sigma_{rr} = -\frac{1}{v_P^2}\ddot{g}\delta(r), \tag{25}$$

whose solution is [6]:

$$\sigma_{rr} = \frac{H(t)}{4\pi r v_P^2} g\left(t - \frac{r}{v_P}\right), \tag{26}$$

where *H* is the Heaviside function. Then, the analytical solution corresponding to the ring is given by:

$$\sigma_{rr} = \frac{H(t)}{4\pi v_P^2} \sum_{i=1}^{N} \frac{1}{r_i} g\left(t - \frac{r_i}{v_P}\right) \tag{27}$$

To calculate the numerical solution, we use one mesh, 74 m wide and 200 m high, discretized with 91 radial grid points and 250 vertical grid points. At the innermost radius, $\epsilon = 50$ cm, the free-surface boundary conditions Eqs. 16, 17, and 18 are applied. As stated above, a dilatational source is applied at $r_0 = 16$ m

and the receiver is located at the same source depth, at 32 m from the axis. The comparison between the analytical and numerical solutions is shown in Fig. 4. The agreement is good and provides a first verification of the modeling algorithm. The phases of the first arrivals are the same because the paths of the signals, in the analytical and numerical cases, are the same. The phases of the second arrivals are opposite because, in the analytical case, the signal arrives from the more distant point source (left side of the ring), while in the numerical case, the signal is reflected by the innermost boundary where the free-surface boundary condition is applied. In fully 3-D media, this will not happen since the singularity at the borehole axis in 3-D space is much smaller than the wavelength and will not be seen by the wave.
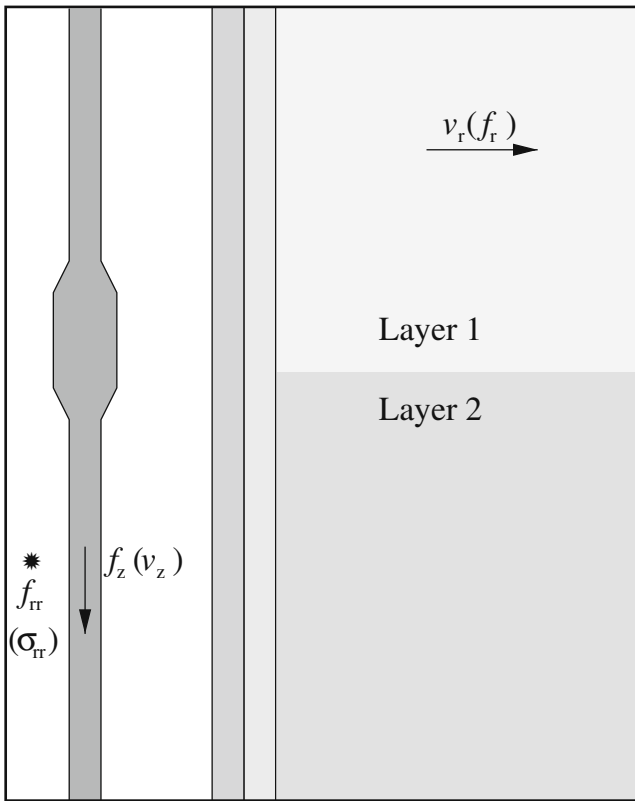
5.2 A reciprocity test

The following numerical experiments test the algorithm by verifying the reciprocity principle. Seismic reciprocity implies that sources and receivers can be interchanged under certain conditions. This relationship holds for a viscoelastic medium with arbitrary boundary conditions, inhomogeneity, and anisotropy (e.g., [10]).

We test reciprocity for selected recording points in the borehole and in the formation. The model is shown in Fig. 5, and consists of a drill string with tool joint immersed in the drilling mud, in the presence of casing, cement, and an inhomogeneous formation. Table 1 shows the acoustic and geometrical properties of the model [8, 22]. The extensions of the four meshes are $r_a - \epsilon$ for the inner mud, $r_b - r_a$ for the tool joint, $r_c - r_b$ for the outer mud, and $r_d - r_c$ for the casing–cement–formation system. In these calculations, we use $n_r = 11$, 11, 11, and 76 grid points with variable grid spacing along the radial direction for the
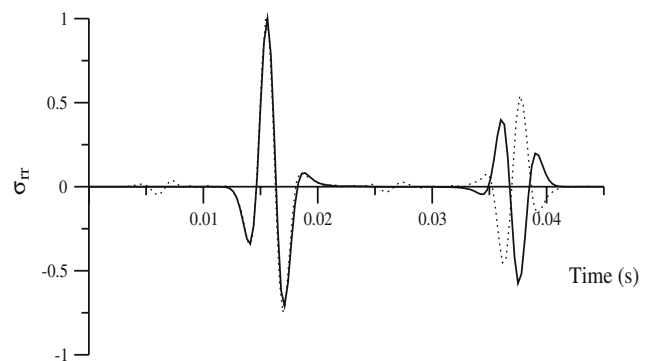
Fig. 4 Comparison between the analytical (*solid line*) and numerical (*dotted line*) solutions (relative amplitude) using the "free-surface" boundary condition at the borehole axis

Fig. 5 Vertical section of the borehole/drill string system used for the reciprocity tests. Note the presence of a tool joint and a layer (see properties in Table 1), and the different horizontal and vertical scales. The first experiment consists of a vertical force f_z applied to the drill string and a receiver that records the radial particle velocity v_r in the formation. The receiver is located at 80 cm from the borehole axis. The reciprocal experiment corresponds to a radial source f_r in the formation and the vertical particle velocity v_z in the drill string. The second experiment consist of an explosive source f_{rr} in the inner mud and a receiver that records the radial particle velocity v_r in the formation. The reciprocal experiment corresponds to a radial source f_r in the formation and the pressure field in the inner mud. The reciprocal experiments are indicated between *parentheses*

four meshes (inner mud, pipe, outer mud, and casing–cement–formation). The minimum grid spacings along the radial direction are 1.2, 0.75, 2.14, and 0.8 mm, for the inner mud, pipe, outer mud, and casing–cement–formation, respectively. The number of grid points in the vertical direction is $n_z = 125$ with a uniform grid spacing of 1.6 cm. A tool joint of 45.5 cm length is located between the vertical grid points 34 and 62. The drill pipe has inner and outer radii equal to 5.5 and 7.6 cm, respectively, and where there is no tool joint, the radial grid points 1 to 3 and 8 to 11 have the drilling-mud properties. The casing and cement correspond to the radial grid points 1 to 3 (0.5 cm thick) and 4 to 6 (1 cm), respectively, of the outer mesh. The horizontal interface is located at the vertical grid points 50 (80 m depth). We perform two tests. First, we compare the radial particle velocity (v_r) measured in the formation due to a vertical force (f_z) in the drill string, to the vertical particle velocity (v_z) at the drill string location due to a radial force (f_r) in the formation. In the second test, we compare the radial particle velocity (v_r) measured in the formation due to an explosive source (f_{rr}) in the inner mud to the pressure (p_r) in the inner mud due to a radial force (f_r) in the formation (e.g., see [1, 6]). The comparisons, corresponding to the first and second experiments, are shown in Fig. 6a, b, respectively, where the dots correspond to the radial source. To avoid numerical noise, we use three point sources along the radial direction, with weight 0.3, 1, and 0.3; the location of the central source is defined as the source location. Source (receiver) and receiver (source) in the first experiment are located at the grid points $(i_r, i_z) =$ (5, 72) (string) and $(i_r, i_z) =$ (38, 37) (formation), corresponding to the coordinates (6.25, 115) and (106, 59) cm, respectively (the radial coordinates refer to the hole axes). The source and the receiver in the inner mud are located at the grid points $(i_r, i_z) = (5, 72)$, corresponding to the coordinates (2, 115) cm. The pulses (Ricker wavelets) have a peak frequency of 14 kHz. The solution is propagated to 3 ms with a time step of 0.04 μs. (The maximum time step is determined by the minimum grid spacing divided by the maximum P-wave velocity.) The agreement is good and provides a further verification of the modeling algorithm.

Table 1 Geometrical and material properties used for the reciprocity test

	v_P (m/s)	v_S (m/s)	ρ (g/cm³)	ϵ (cm)	r_a (cm)	r_b (cm)	r_c (cm)	r_d (cm)
Inner mud	1,520	0	1	0.16	5.5	–	–	–
Tool joint	5,900	3,190	7.85	–	5.2	8.25	–	–
Drill pipe	5,900	3,190	7.85	–	5.5	7.6	–	–
Outer mud	1,520	0	1	–	–	8.25	17	–
Casing	5,900	3,190	7.85	–	–	–	–	–
Cement	4,400	2,100	2	–	–	–	–	–
Layer 1	3,200	1,850	2.6	–	–	–	17	200
Layer 2	2,200	1,300	2.4	–	–	–	17	200

Fig. 6 Test of the algorithm using the reciprocity principle, where **a** corresponds to the first experiment described in Fig. 5 (vertical force in drill string), and **b** corresponds to the second experiment described in Fig. 5 (dilatational source in inner mud). The *solid line* is the radial particle velocity measured at the formation, while the *dots* correspond to the pressure and particle velocity measured at the inner mud (**a**) and at the drill string (**b**) (see Fig. 5)
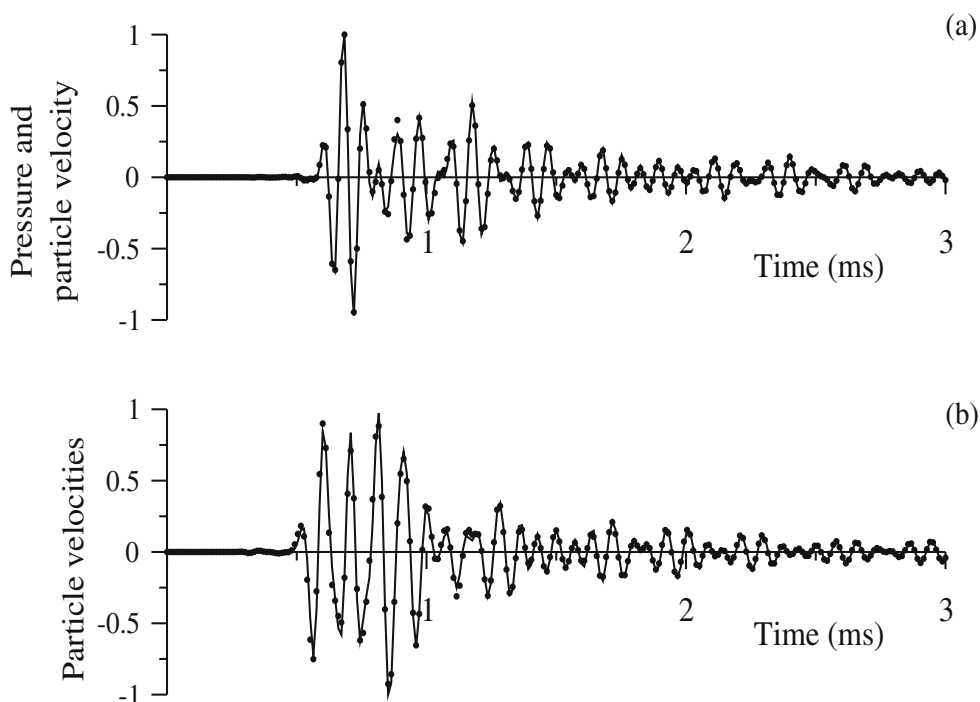
5.3 Simulation of propagation modes

Next, we simulate wave propagation in a fluid-filled borehole in the presence of drill string and surrounded by two different formations. The properties of the two formations, hard and soft, are given in Table 2. The hard formation shear speed corresponds to sandstone and that of the soft formation to shales and clays. The shear wave velocity v_S of these formations is higher (hard) and lower (soft) than the acoustic mud velocity. The compressional wave velocity is assumed to be $\sqrt{3}$ times the shear velocity (Poisson's ratio = 1/4) in both cases. The numerical meshes have $n_r = 11, 11, 11$, and 91 grid points in the radial direction for the inner mud, drill string, outer mud, and formation, respectively. The extension of the outer grid is $r_d = 20$ m. The model depth is 200 m discretized with $n_z = 375$ grid points and a uniform grid spacing of 0.5 m. The perturbation is a vertical force with a peak frequency of 375 Hz. It is applied to the drill string at the radial grid points

4, 5, and 6, with weight 0.3, 1, and 0.3, respectively, and to the vertical grid point 300. Vertically polarized receivers are located at the radial grid points 5, 5, and 5, for the inner mud, drill string, and outer mud, respectively, and at the radial grid points 2, 5, and 46 in the formation (16 cm, 25 cm, and 10 m away from the borehole axis, respectively). The solution is propagated to 35 ms with a time step of 90 ns, and the output time traces are resampled to 27 μs. The simulation uses the material properties and dimensions given by Rama Rao and Vandiver [19], which are summarized in Table 2.

There are three propagating modes for frequencies below 1 kHz [19]. The first mode (M1) is the extensional wave traveling in the drill string. It has a velocity close to that of the axial waves traveling along a steel rod in air. This mode is nondispersive up to 1 kHz and insensitive to the properties of the drilling fluid and formation. The second mode (M2) has a velocity close to that of plane waves in fluids confined in an elastic pipe

Table 2 Geometrical and material properties used to simulate borehole waves

|	v_P (m/s)	v_S (m/s)	ρ (g/cm^3)	ϵ (cm)	r_a (cm)	r_b (cm)	r_c (cm)	r_d (m)
Inner mud	1,558	0	1	0.26	5.32	–	–	–
Drill pipe	5,900	3,400	7.8	–	5.32	6.35	–	–
Outer mud	1,558	0	1	–	–	6.35	15.2	–
Hard formation	3,279	1,893	2	–	–	–	15.2	20
Soft formation	1,409	813	2	–	–	–	15.2	20

and its characteristics are determined mainly by the properties of the inner mud and pipe and very weakly by the media outside the pipe. The third mode (M3), strongly influenced by the formation, is equivalent to the Stoneley wave traveling in boreholes without pipe (commonly termed "tube wave").

Approximate expressions of the phase velocity of the various modes at low frequencies are given in the following. Kolsky [11] provides the velocity of the M1 mode (rod mode) as a function of the wavelength, but since the wavelength itself is a function of the phase velocity, this results in a cubic equation for the phase velocity vs the frequency f:

$$c_1^3 - c_0(c_1^2 - v^2) = 0, \qquad v = \pi f \nu r_b, \qquad (28)$$

where $c_0 = (Y/\rho)^{1/2}$, with ρ and $Y = \mu(3\lambda + 2\mu)/(\lambda + \mu)$ the density and Young modulus of the pipe, $\nu = \lambda/[2(\lambda + \mu)]$ is the Poisson ratio, and r_b is the radius of the rod. The group velocity is given by $3c_1 - 2c_0$ [11]. Using the values in Table 1 and $f = 600$ Hz we obtain, for mode M1, $c_0 = 5{,}131$ m/s, $c_1 = 5{,}130$ m/s, and a group
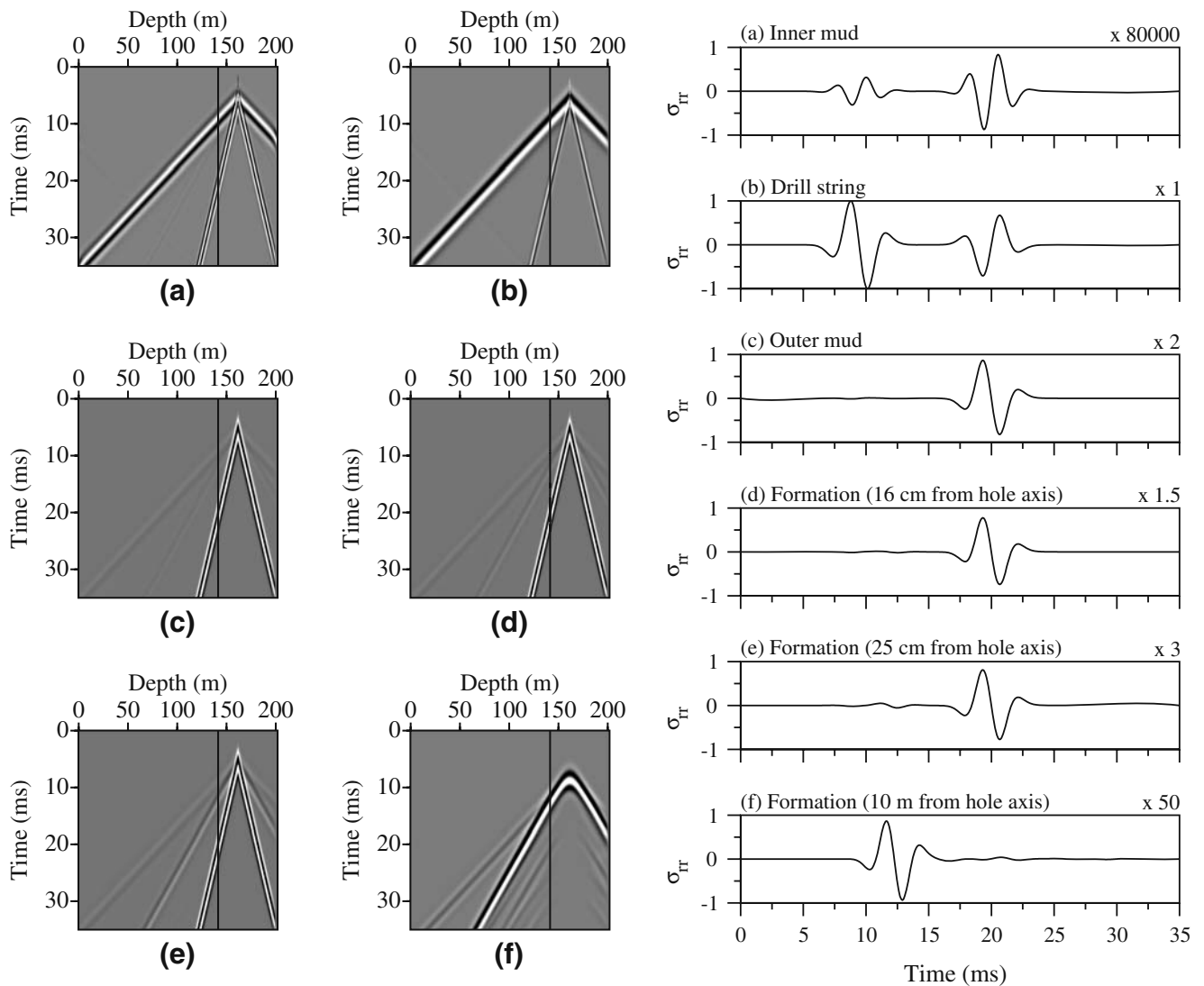
Fig. 7 Hard formation. The *left side of the panel* shows the VSP of the pressure field calculated at constant radial locations in the center of the mesh corresponding to the inner mud (**a**), string (**b**), outer mud (**c**), and three different locations in the formation [16 cm (**d**), 25 cm (**e**), and 10 m (**f**) from the hole axis]. The *vertical line* indicates the location of the seismograms shown in the *right side of the panel*, that represent the pressure field measured in the borehole 20 m above the source. The source is a vertical force applied in the pipe at a depth of 160 m. The *numbers* in the upper right side of each seismogram are the scale factors of the amplitude computed in each medium with respect to the amplitude in the drill string

velocity of 5,130 m/s. At $f = 10$ kHz, the phase and group velocities are 5,040 and 4,859 m/s, respectively.

The velocity of the M2 mode is given by:

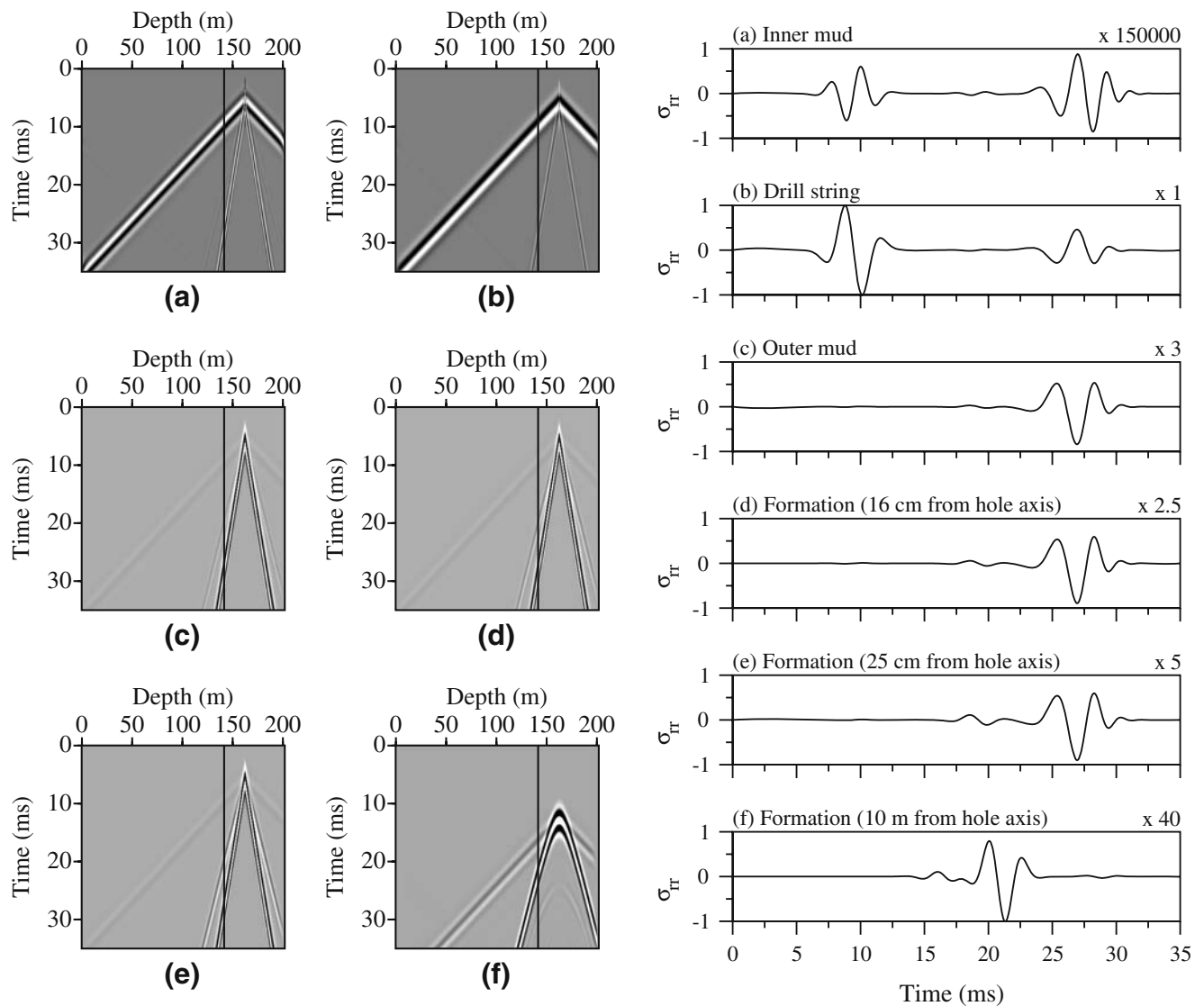$$c_2 = \left[\rho_f \left(\frac{1}{\lambda_f} + \frac{1}{M} \right) \right]^{-1/2}, \tag{29}$$

where

$$M = \frac{Y(r_b^2 - r_a^2)}{2[(1+\nu)r_b^2 + (1-\nu)r_a^2]}, \tag{30}$$

r_b and r_a are the outer and inner radii of the pipe, ρ_f and λ_f are the density and bulk modulus of the mud, and ν is the Poisson ratio of the pipe [21]. Therefore, using the values in Table 1, we obtain $c_2 = 1,464$ m/s for $r_a = 5.5$ cm and $r_b = 7.6$ cm.

Finally, the velocity of the M3 mode without pipe and in the presence of casing is [16]:

$$c_3 = \left[\rho_f \left(\frac{1}{\lambda_f} + \frac{1}{N} \right) \right]^{-1/2}, \tag{31}$$

Fig. 8 *Soft formation*. The *left side of the panel* shows the VSP of the pressure field calculated at constant radial locations in the center of the mesh corresponding to the inner mud (**a**), string (**b**), outer mud (**c**), and three different locations in the formation [16 cm (**d**), 25 cm (**e**), 10 m (**f**) from the hole axis]. The *vertical line* indicates the location of the seismograms shown in the *right* side of the panel, that represent the pressure field measured in the borehole 20 m above the source. The source is a vertical force applied in the pipe at a depth of 160 m. The numbers in the upper right side of each seismogram are the scale factors of the amplitude computed in each medium with respect to the amplitude in the drill string

$$N = \frac{2(1 - \nu)\mu_F + (\mu - \mu_F)(1 - a^2)}{2(1 - \nu) - (1 - \mu_F/\mu)(1 - 2\nu)(1 - a^2)} \qquad (32)$$

where $a = r_c/r_c'$, with r_c and r_c' the inner and outer radii of the casing, μ_F the formation shear modulus, and μ and ν the shear modulus and Poisson ratio of the steel casing. At infinite shear-wave velocity, the tube-wave velocities approach the sound speed of mud (the limit is not exact for Marzetta and Schoenberg's equation). At zero shear-wave velocity, cased boreholes have a finite tube-wave velocity, while the velocity in uncased boreholes is zero. The cased-hole and uncased-hole velocities c_3 are 1,413 and 1,354 m/s, respectively, for the formation properties given in Table 1. Using the values

of Table 2, the velocities of modes M1 and M2, which do not depend on the formation type, are 5,379 and 1,467 m/s, respectively, while the velocity of mode M3 is 1,389 m/s for the hard formation and 942 m/s for the soft formation, considering frequencies below 1 kHz. The simulations are performed by tuning the parameters to avoid instabilities, which may arise because of large differences in the radial and vertical dimensions of the cells and strong impedance contrasts.

Figures 7 and 8 show the VSP of the pressure field recorded in the inner mud, string, outer mud, and formation, hard and soft, respectively, and VSP seismograms at 20 m above the source. The constant wave delay is about 3 ms. The amplitudes of the signals,

Fig. 9 Propagation in the presence of a horizontal interface separating two layers. VSP of the pressure field calculated at constant radial locations in the center of the mesh corresponding to the inner mud (**a**), string (**b**), outer mud (**c**), and three different locations in the formation [16 cm (**d**), 25 cm (**e**), 10 m (**f**) from the hole axis]. In the lowest part of the panel is shown a blow up of the oversaturated VSP detected in the string (**b**). It is possible to observe the presence of weak signals in the drill pipe due to the reflections from the layers
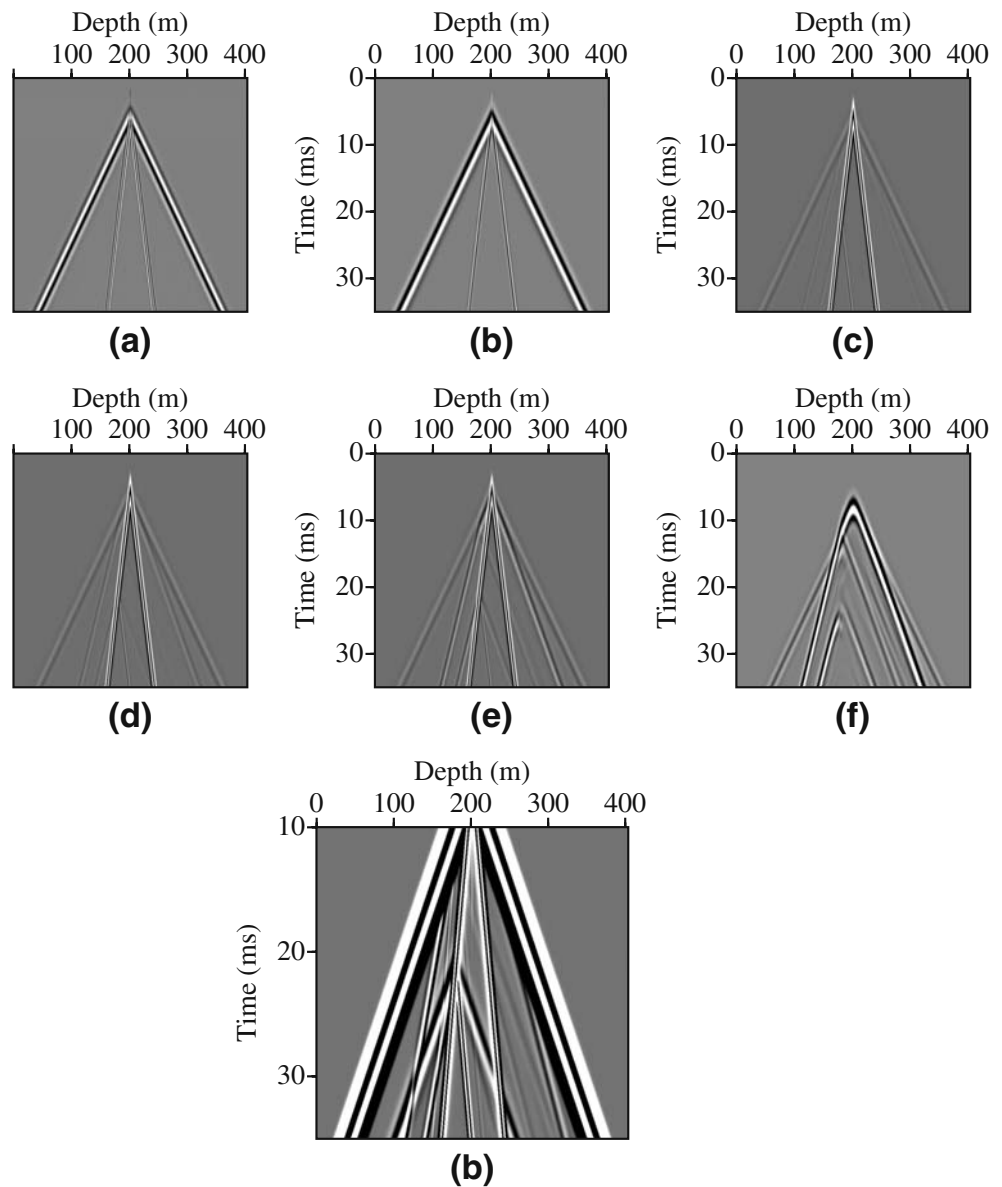
computed in the inner mud and outer mud and at three different points in the hard and soft formations, are lower than the amplitude in the drill string. The scale factors are shown in the upper right side of each seismogram.

M1 is the dominant mode in the drill string and the measured velocity is approximately 5,380 m/s, its amplitude is about 40 times greater than that detected in the hard formation and 80 times greater than that detected in the soft formation in a receiver close to the borehole wall. These scale factors are so high that the mode is not visible in the seismograms acquired at the formations where mode M3 is the dominant mode with amplitude only lower than that detected in the drill pipe (see the right panel of Figs. 7 and 8). The ratio between the amplitudes detected in the pipe and in the formations increases with the distance from the borehole axis.

The velocity of mode M3, measured by picking the maximum of the energy, is 1,340 m/s, in the model with a hard formation, while this velocity is 921 m/s in the inner mud and 946 m/s in the outer mud, in the model with a soft formation. Modes M2 and M3 are difficult to distinguish since their velocities are very similar, especially in the presence of the hard formation. The amplitude of the signal observed in the inner mud, in the presence of both formations, is more than four orders of magnitude weaker than that in the pipe.

In both formations, it is possible to observe waves radiated by the borehole system and interpreted as head waves. In the soft formation, the pipe waves are weaker than that observed in the hard formation and decay away from the hole axis (see Fig. 8f), while in the hard formation, such waves are still present at 10 m from the hole axis (see Fig. 7f). In the soft formation, where the velocity of the formation is subsonic, it is possible to observe, separately, mud waves radiated by the inner and the outer mud (see Fig. 8d, e).

In order to study the effects of formation discontinuity, we simulate the wave propagation in the presence of two half-spaces in contact, defining a horizontal interface in the formation. As the reciprocity example shown in Fig. 5, this problem cannot be solved by using analytical methods such as the one used by Rama Rao and Vandiver [19]. The model geometry and acoustic properties for the drilling mud and pipe are given in Table 2. The upper layer, extending until a depth of 180 m, has $v_P = 2,800$ m/s, $v_S = 1,620$ m/s, and $\rho = 2$ g/cm^3. The lower layer has $v_P = 4,200$ m/s, $v_S = 2,450$ m/s, and $\rho = 2.2$ g/cm^3. The results are shown in Fig. 9. Weak events, due to the formation discontinuity, can be observed in the drill pipe, with amplitudes thousand times lower than the dominant signal.

6 Conclusions

We simulate axis-symmetric waves in boreholes with inner mud, nonuniform pipes, outer mud, and formation. The media is uniform along the azimuthal direction, but there are no restrictions along the vertical and radial directions, where any type of inhomogeneity can be modeled. The algorithm allows us to model in detail the nonuniform drill string and simulate the different propagating modes along the borehole-formation system. We observe the dominant mode M1 in the drill pipe in both (hard and soft) formations with a velocity close to the theoretical one. In the formations, we observe the mode M3 together with the pipe waves (interpreted as head waves). The algorithm is tested by comparison to an analytical solution and reciprocity tests, and the computations agree with the low-frequency results obtained by using more simplified analyses reported by other authors.

References

1. Arntsen, B., Carcione, J.M.: A new insight into the reciprocity principle. Geophysics **65**, 1604–1612 (2000)
2. Boyd, J.P.: Chebyshev and Fourier Spectral Methods. Dover, New York (2001)
3. Carcione, J.M.: Domain decomposition for wave propagation problems. J. Sci. Comput. **6**, 453–472 (1991)
4. Carcione, J.M.: A 2-D Chebyshev differential operator for the elastic wave equation. Comput. Methods Appl. Mech. Eng. **130**, 33–45 (1996)
5. Carcione, J.M.: Modeling elastic waves in the presence of a borehole and free surface. In: 64th Ann. Internat. Mtg., Soc. Expl. Geophys., Expanded Abstracts (1994)
6. Carcione, J.M.: Wave Fields in Real Media. Theory and Numerical Simulation of Wave Propagation in Anisotropic, Anelastic, Porous and Electromagnetic Media (Second edition, revised and extended). Elsevier, Amsterdam (2007)
7. Carcione, J.M., Helle, H.B.: On the physics and simulation of wave propagation at the ocean bottom. Geophysics **69**, 825–839 (2004)
8. Carcione, J.M., Poletto, F.: Simulation of stress waves in attenuating drill strings, including piezoelectric sources and sensors. J. Acoust. Soc. Am. **108**, 53–64 (2000)
9. Fornberg, B.: A Practical Guide to Pseudospectral Methods. Cambridge University Press, Cambridge (1996)
10. Fung, Y.C.: Foundations of Solid Mechanics. Prentice-Hall, Engelwood Cliffs (1965)
11. Kolsky, H.: Stress Waves in Solids. Dover, New York (1963)
12. Lea, S.-H., Kyllingstad, A.: Propagation of coupled pressure waves in borehole with drillstring. Society of Petroleum Engineers, paper no. 37156 (1996)

13. Lee, H-Y: Drillstring axial vibration and wave propagation in boreholes. Ph.D. Thesis, M.I.T. (1991)
14. Kessler, D., Kosloff, D.: Acoustic wave propagation in 2-D cylindrical coordinates. Geophys. J. Int. **103**, 577–587 (1990)
15. Kessler, D., Kosloff, D.: Elastic wave propagation using cylindrical coordinates. Geophysics **56**, 2080–2089 (1991)
16. Marzetta, T.L., Schoenberg, M.: Tube waves in cased boreholes. In: 55th Ann. Internat. Mtg., Soc. Expl. Geophys. Expanded Abstracts, 34–36 (1985)
17. Poletto, F., Carcione, J.M., Lovo, M., Miranda, F.: Acoustic velocity of SWD borehole guided waves. Geophysics **67**, 921–927 (2002)
18. Poletto, F., Miranda, F.: Seismic While Drilling. Fundamentals of Drill-bit Seismic for Exploration. Elsevier, Amsterdam (2004)
19. Rama Rao, V.N., Vandiver, J.K.: Acoustics of fluid filled boreholes with pipe: guided propagation and radiation, J. Acoust. Soc. Am. **105** 3057–3066 (1999)
20. Randall, C.J., Scheibner, D.J., Wu, P.T.: Multipole borehole acoustic waveforms: synthetic logs with beds an borehole washouts. Geophysics **56**, 1757–1769 (1991)
21. White, J.E.: Seismic Waves: Radiation, Transmission and Attenuation. Mc-Graw Hill, New York (1965)
22. Winbow, G.A.: Seismic sources in open and cased boreholes. Geophysics **56**, 1040–1050 (1991)